NANOSYSTEMS:
PHYSICS, CHEMISTRY, MATHEMATICS

Navarro-Vilca S., et al. *Nanosystems: Phys. Chem. Math.*, 2024, **15** (5), 597–620.
http://nanojournal.ifmo.ru

Original article

DOI 10.17586/2220-8054-2024-15-5-597-620

Skyrmionium – semicircular magnetic defect interaction on a racetrack

S. Navarro-Vilca[1,a], S. Urcia-Romero[2,b], H. Vigo-Cotrina[3,c]

[1]Universidad Nacional Jorge Basadre Grohmann, Tacna, Perú
[2]University of Puerto Rico, Mayaguez Campus, Puerto Rico, USA
[3]Universidad Privada del Norte, Trujillo, Perú

[a]srnavarrov@unjbg.edu.pe, [b]silvana.urcia@upr.edu, [c]helmunt.vigo@upn.edu.pe

Corresponding author: H. Vigo-Cotrina, helmunt.vigo@upn.edu.pe

ABSTRACT Different types of skyrmionics magnetic configurations can be created and manipulated on different types of nanostructures. In this research, we use micromagnetic simulations to study the dynamics of a skyrmionium on a racetrack in the presence of a semicircular magnetic defect. We considered a defect with physical parameters different from those of the racetrack itself. Our results show that, depending on the size of the defect, the width of the racetrack, and the intensity of the spin current density, it is possible to manipulate the trajectory of a skyrmionium. Also, we obtain the interaction energies between the skyrmionium and the magnetic defect and derive phase diagrams showing the different dynamic states that can be obtained during the movement of the skyrmionium.

KEYWORDS skyrmionium, micromagnetic simulation, target skyrmion

FOR CITATION Navarro-Vilca S., Urcia-Romero S., Vigo-Cotrina H. Skyrmionium – semicircular magnetic defect interaction on a racetrack. *Nanosystems: Phys. Chem. Math.*, 2024, **15** (5), 597–620.

1. Introduction

Skyrmions are considered exotic magnetic configurations characterized by a topological charge $Q = \pm 1$ [1–5]. They can be created in different types of nanostructures [6–9]. Skyrmions have a central region (skyrmion core) where the magnetization can point along the $+z$ axis ($Q = +1$) or along the $-z$-axis ($Q = -1$) [2, 8, 10–12].

Due to their topological charge, skyrmions are affected by the skyrmion Hall effect (SkHE) when they are moving along the length of a racetrack, which causes the skyrmion not to maintain its original path and to be annihilated at the edges of the racetrack.

Another possible problem for potential applications is the presence of defects and/or impurities within the nanostructure due to inherent manufacturing processes. Therefore, some investigations show how a skyrmion interacts in the presence of a magnetic defect [8, 13–18]. Combining a skyrmion with $Q = +1$ and a skyrmion with $Q = -1$ gives the magnetic configuration of a 2π skyrmion with topological charge $Q = 0$ [3, 8, 19]. This configuration, also known as target skyrmion [20] or skyrmionium is not affected by the SkHE, which allows the skyrmionium to move in a straight line without suffering any deviation, thus avoiding the possibility of being destroyed at the edges of a racetrack [3, 8, 19].

Skyrmioniums can be created in nanostructures using external agents, such as spin-polarized currents [3, 8, 21, 22] or magnetic fields [20, 23–25]. These external agents can also induce skyrmionium movement, as shown in various works [3, 4, 19, 21, 22, 26]. It is also possible to move a skyrmionium using an anisotropy gradient [27]. The translational speed of a skyrmionium can be much higher than that of a skyrmion, making it more desirable for potential applications in the field of spintronics [3, 19, 25].

Skyrmioniums can collapse into a skyrmion due to random thermal fluctuations following a core annihilation process as shown by Jiang et al. [28]. Furthermore, other more complex magnetic configurations, such as the heliknoton, may also be sensitive to thermal fluctuations and collapse [29]. Such transitions are of importance and still open for future research.

In our previous work [30], we studied the dynamics of a skyrmionium on a racetrack in the presence of a magnetic defect with its physical parameter $D_{\text{int}}^{\text{def}}$. However, in an actual situation, the defect may have other physical parameters different from those of the racetrack, such as exchange constant ($A_{\text{ex}}^{\text{def}}$), saturation magnetization (M_s^{def}), and perpendicular uniaxial anisotropy constant (K_z^{def}). As has been shown by Can Önel et al. [21], even the racetrack's width can influence the skyrmionium's dynamics. In that sense, we expanded our recently published work, considering that the magnetic defect can have different physical parameters with respect to the racetrack. Lastly, we studied the influence of defect size and racetrack width on the skyrmionium dynamics.

2. Method

All simulations were carried out using the open-source program MuMax3, which numerically solves the Landau–Lifshitz–Gilbert (LLG) equation [31]:

$$\dot{m} = -\gamma_e m \times B_{\text{eff}} + \alpha m \times \dot{m} + \gamma_e \epsilon \beta \left[(m \times s) \times m \right],$$

where m is the reduced magnetization, B_{eff} is the effective field, γ_e=1.76 $\times$ 10^{11} $\text{T}^{-1}\text{s}^{-1}$ is the electron gyromagnetic ratio, the last term of the equation is related to the torque exerted by the current on magnetization. The constants are detailed and defined in references [3, 16].

We simulated a ferromagnetic cobalt racetrack with a width of $W = 512$, 256, and 128 nm, and a thickness of 1 nm coupled to a heavy metal material (HM) (see Fig. 1). The racetrack was discretized into $2 \times 2 \times 1$ nm^3 cells, using the following typical parameters for cobalt [3, 8, 13]: saturation magnetization $M_s = 580$ kA/m, exchange constant $A_{\text{ex}} = 15$ pJ/m, DMI constant $D_{\text{int}} = 3.4$ mJ/m^2, perpendicular uniaxial anisotropy constant $K_z = 0.8$ MJ/m^3 and damping constant $\alpha = 0.3$.

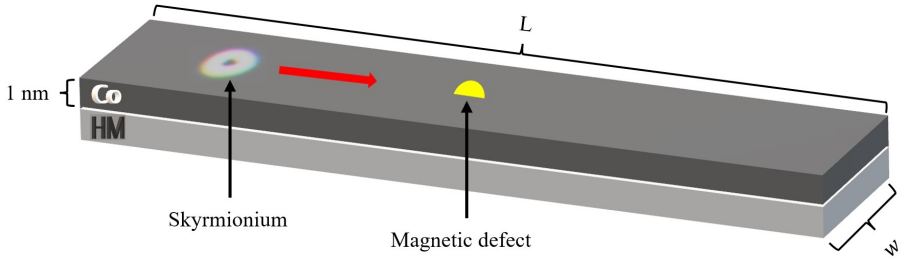

FIG. 1. Schematic representation of the cobalt racetrack coupled to a heavy metal material. The red arrow indicates the direction of movement of the skyrmionium

For these values, the racetrack supports three magnetic configurations: a perpendicular domain, a skyrmion, or a skyrmionium. The perpendicular domain state is the ground state. However, a skyrmionium can be created in the racetrack using any of the methods used in the literature [3,8,20–23,25]. The inner and outer diameters have values of approximately 8 and 75 nm, respectively. The widths of the inner and outer domain walls have values of approximately 6 and 12 nm. Both the values of the diameters and the widths of the domain walls remain approximately constant for all widths W.

A semicircular magnetic defect was located in the center of the racetrack. We considered defects with diameters $\rho = 20$, 30, and 40 nm and the following physical values: DMI constant $D_{\text{int}}^{\text{def}}$ varying between 3.0 and 3.8 mJ/m^2 in increments of 0.1 mJ/m^2, saturation magnetization M_s^{def} varying between 540 and 620 kA/m in increments of 10 kA/m, exchange constant $A_{\text{ex}}^{\text{def}}$ varying between 11 and 19 pJ/m with increments of 1 pJ/m, and uniaxial anisotropy constant K_z^{def} varying between 0.4 and 1.2 MJ/m^3 in increments of 0.1 MJ/m^3 .

3. Results and discussions

The interaction energy $E_{\text{int}}(x)$, where x is the position of the defect along the length of the racetrack between the magnetic defect and the skyrmionium, was calculated using the expression [16]:

$$E_{\text{int}}(x) = E(x) - E(x \to \infty). \tag{1}$$

Figure 2 shows the interaction energy values for different physical parameters of the defect with a diameter of $\rho = 40$ nm and width of $W = 512$ nm. The figure shows that the interaction energy is repulsive (see Fig. 2(a) and Fig. 2(g)) when the values of the physical parameters $D_{\text{int}}^{\text{def}}$ and M_s^{def} of the defect are less than the values of D_{int} and M_s of the racetrack and attractive (see Fig. 2(b) and Fig. 2(h)) when these parameters are greater than those of the racetrack. On the other hand, the interaction energy is attractive (see Fig. 2(c) and Fig. 2(e)) when the physical parameters $A_{\text{ex}}^{\text{def}}$ and K_z^{def} are lower than the values of A_{ex} and K_z of the racetrack and repulsive ((see Fig. 2(d) and Fig. 2(f))) when they are larger than those of the racetrack. The same behavior is observed for all defect diameters and widths W considered in this work (see Figs. A1–A9 in Appendix). Also these figures show that the absolute value of the interaction energy decreases with decreasing defect size and increases with increasing diameter. Defects with minimal diameters will have a negligible effect on the dynamics of the skyrmionium.

In some cases, small oscillations in the interaction energy values are observed near the position $x = 0$. These oscillations may occur due to the defect having an asymmetric shape. Additionally, when a skyrmionium comes into contact with the defect (with its own specific physical parameters) it can deform, causing oscillations.

Interestingly, for all M_s^{def} values used in this research, the interaction energy is an order of magnitude lower than for the other cases. This fact suggests that modifying this parameter will have a negligible effect on the dynamics of the skyrmionium, which will be evidenced in the next section.

In Appendix, we have added figures (Fig. A20–A22) showing the interaction energy for the case of a skyrmion, using $W = 512$ nm. These figures show that the same physical principles that apply for the skyrmionium also apply to the skyrmion, i.e., the same repulsive and attractive potentials appear for the same physical parameters of the defect. On the other hand, we can see that the intensity of the interaction energy, in some cases, is almost the same.

Next, to study the dynamics of the skyrmionium in the presence of the magnetic defect, a skyrmionium is created to the left of the defect (see Fig. 1). The movement of the skyrmionium is induced via the Spin Orbit Torque effect (SOT). That is, a current density flowing in the HM material along the x-axis generates a current density in the racetrack with spin polarization in the $-y$ direction. We consider J values between 1 and 9 MA/cm^2 in increments of 0.5 MA/cm^2.

3.1. Magnetic defect with different $D_{\text{int}}^{\text{def}}$

Figure 3 shows phase diagrams with three possible states: (i) the skirting state, in which the skyrmionium manages to avoid the defect by skirting it (see Fig. A13 in Appendix); (ii) the passing state, where the skyrmionium crosses the defect while maintaining approximately its original trajectory (see Fig. A14 in Appendix); and (iii) the pinning state, trapping the skyrmionium inside the defect (see Fig. A15 in Appendix). The maximum deviation in the passing state, obtained for the parameters used in this work, was less than 10 nm below its original trajectory, which is negligible compared to the size of the racetrack.

When $D_{\text{int}}^{\text{def}} < D_{\text{int}}$, there are two possible states: skirting and passing. The number of skirting states increases with increasing defect diameter size. The maximum number of skirting states for each diameter occurs when the difference between D_{int} and $D_{\text{int}}^{\text{def}}$ is largest ($D_{\text{int}}^{\text{def}} = 3$ mJ/m^2). When $D_{\text{int}}^{\text{def}} = 3$ mJ/m^2, the minimum value of the current density $J_{\min}$ is necessary to overcome the repulsion by the defect is 2.5 MA/cm^2 for a diameter of 20 nm. When the diameter size increases to 30 and 40 nm, the value of $J_{\min}$ also increases to 4 and 5.5 MA/cm^2, respectively. This behavior is explained by the repulsive interaction energy becomes more intense with increasing defect diameter (see Figs. A1–A3 in Appendix); therefore, a higher value of current J is needed to overcome the interaction.

When the value of $D_{\text{int}}^{\text{def}}$ is reduced to 3.3 mJ/m^2, the repulsive interaction energy becomes smaller; therefore, the value of $J_{\min}$ necessary to overcome it also decreases. In our case, the skyrmionium crosses the magnetic defect for all current density values considered in this work for $\rho = 20$ and 30 nm. For $\rho = 40$ nm, there is a $J_{\min}$ value of 1.5 MA/cm^2

When $D_{\text{int}}^{\text{def}} > D_{\text{int}}$, there are two possible states: passing and pinning. In this case, the interaction energy is attractive; therefore, the defect tends to attract the skyrmionium towards it, thus acting as a trap. This energy becomes higher with the defect's increasing diameter. Therefore, the current values necessary to counteract the pinning effect must also increase. For example, when $D_{\text{int}}^{\text{def}} = 3.8$ mJ/m^2, $J_{\min}$ has a value of 3 MA/cm^2 when $\rho = 20$ nm, while it has a value of 3.5 MA/cm^2 when $\rho = 40$ nm.

3.2. Magnetic defect with different $A_{\text{ex}}^{\text{def}}$

Figure 3 also shows two new states in addition to the three states mentioned above. We dub the two new states TA and TB. In TA (see Fig. A16 in Appendix), the skyrmionium collapses into the defect, transforming into a skyrmion and becoming trapped within the defect. The TB state (see Fig. A17 in Appendix) is similar to the TA state, with the difference that the created skyrmion continues to advance deviating towards the edges of the racetrack due to the SkHE effect. The transformation from skyrmionium to skyrmion is also possible because the racetrack parameters allow the existence of a skyrmion, as mentioned above.

For $\rho = 20$ nm, $A_{\text{ex}}^{\text{def}} = 11$ pJ/m, and $J < 3.5$ MA/cm^2, the skyrmionium will be trapped due to the robust and attractive interaction of the defect and the low influence of the drag force produced by the current. As the current increases ($J \geq 3.5$ MA/cm^2), the driving force on the skyrmionium also increases, causing it to collapse and become a skyrmion. Furthermore, due to the balance between the defect's driving force and attractive force, the skyrmion will be trapped inside the defect (TA state). This behavior can be seen in Fig. 3. For values of $A_{\text{ex}}^{\text{def}} > 11$ and < 14 pJ/m, the dynamic states of the skyrmionium are similar to $A_{\text{ex}}^{\text{def}} = 11$ pJ/m, but depending on the value of J, the skyrmion will manage to overcome the well of the attractive potential, crossing the defect (TB state). The movement of the skyrmion is affected by the (SKHE) ($\theta_{sk} \sim 63.43^\circ$), causing it to move near the edges of the racetrack, as shown in Fig. A17 in Appendix. When the diameter of the defect increases, the attractive interaction becomes more intense; therefore, the number of pinning states also increases (see Fig. 3).

For values of $A_{\text{ex}}^{\text{def}} > 15$ pJ/m, depending on the competition between the force exerted by the current and the repulsive force exerted by the defect, the skyrmionium will avoid the defect by passing around it or will pass through it. When the diameter of the defect increases, the repulsive interaction energy also increases, favoring the appearance of skirting states (see Fig. 3)

For a value of $A_{\text{ex}}^{\text{def}} = 17$ pJ/m, a minimum value of $J = 2.5$ MA/cm^2 is necessary for the skyrmionium to overcome the repulsion generated by the defect when the diameter of the defect is 20 nm. When the diameter increases to 40 nm, the value of J also increases to 4 MA/cm^2.

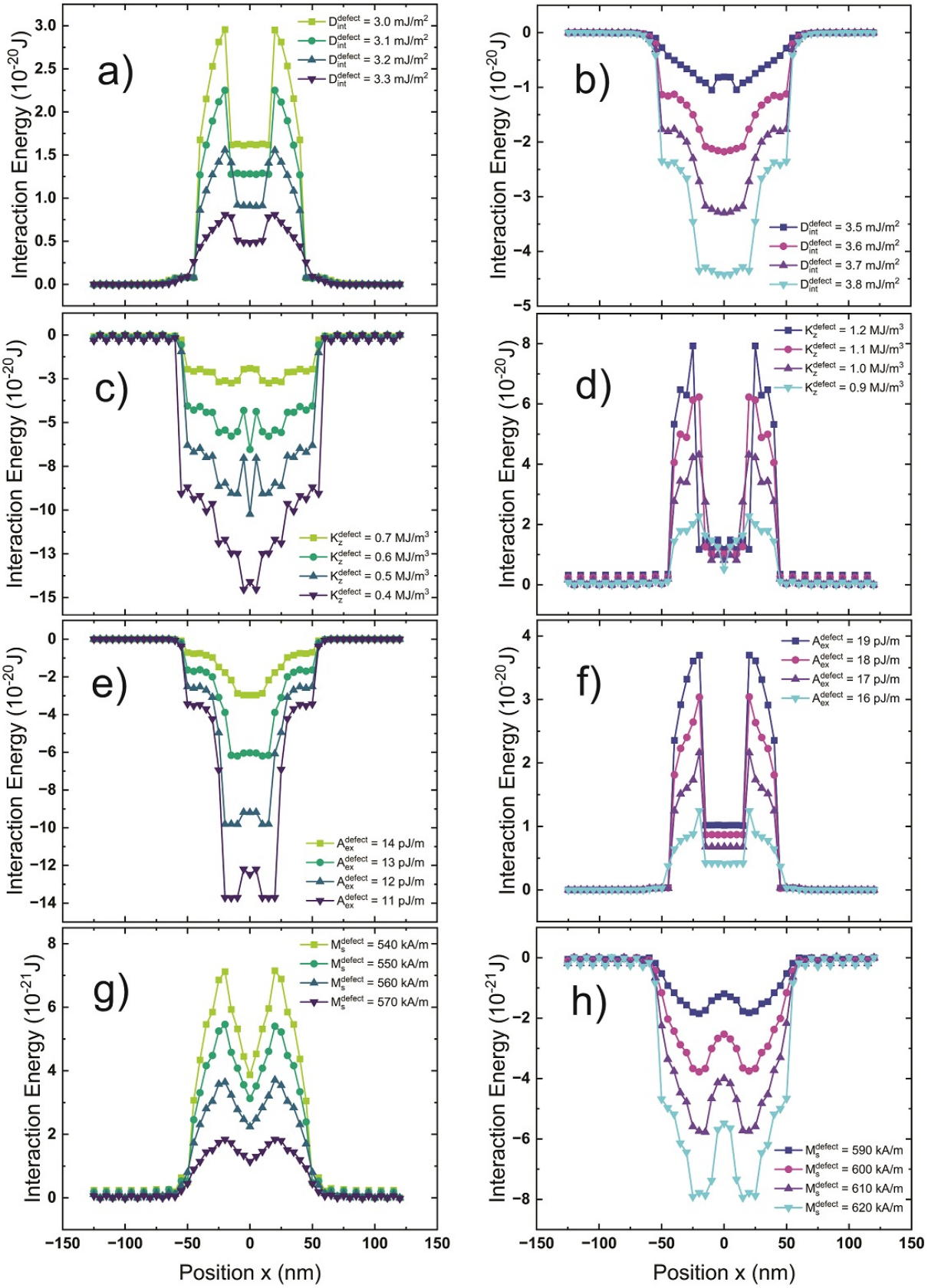

FIG. 2. Interaction energy between the skyrmionium and the defect ($\rho = 40$ nm) obtained by micromagnetic simulation using eq. (1) considering different parameters with a width of $W = 512$ nm

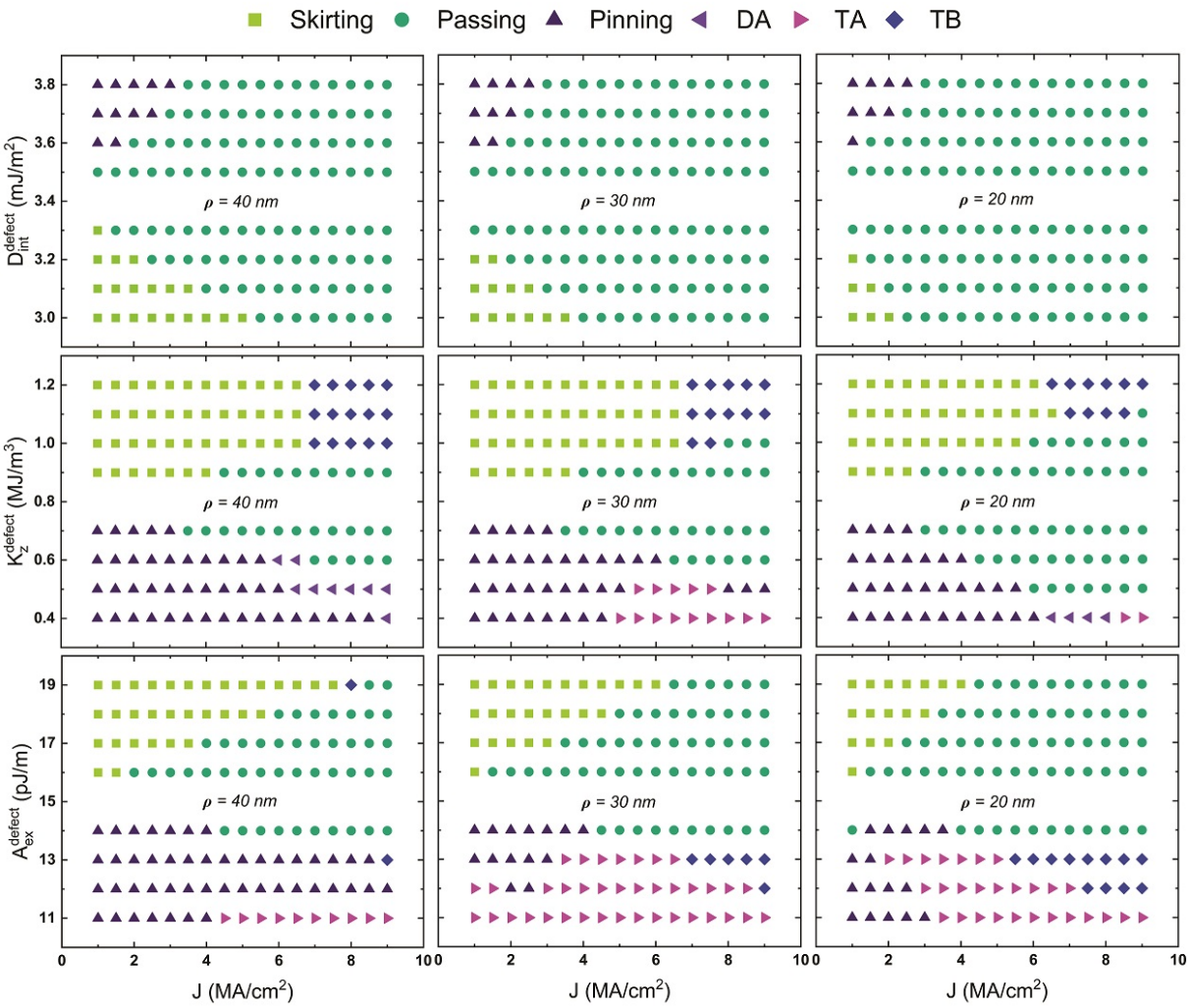

FIG. 3. The phase diagrams of possible states for the skyrmionium dynamics in the presence of a magnetic defect depict a wide range of physical parameters and diameters, offering a comprehensive view of the system's behavior for a width $W = 512$ nm

3.3. Magnetic defect with different K_z^{def}

In this case, a new state we dub as DA (see Fig. A18 in Appendix) appears where the skyrmionium is trapped by the defect; however, due to the current's effect, it deforms, increasing its size along the racetrack.

The interaction is attractive for values of $K_z^{\text{def}} < K_z$, promoting the pinning states until the current can overcome the attraction. For example, when $\rho = 20$ nm and $K_z^{\text{def}} = 0.7$ MJ/m^3, the skyrmionium crosses the defect (passing state) from a minimum value $J_{\min} = 3$ MA/cm^2. However, when the value of ρ increases to 40 nm, the value of $J_{\min}$ also increases to 3.5 MA/cm^2. This effect is even more pronounced for a value of $\rho = 20$ nm and $K_z^{\text{def}} = 0.6$ MJ/m^3. The skyrmionium crosses the defect (passing state) from a minimum value of $J_{\min} = 4.5$ MA/cm^2, but for $\rho = 40$ nm, $J_{\min}$ increases to 7 MA/cm^2.

For values of $K_z^{\text{def}} > K_z$, the interaction between the defect and the skyrmionium becomes repulsive, favoring the appearance of skirting and passing states depending on the value of the current density. In some cases, depending on the competition between the repulsive interaction and the driving force exerted by the current, there are states where the skyrmionium collapses to a skyrmion but continues to move along the racetrack.

3.4. Magnetic defect with different M_s^{def}

Figure A12 in Appendix shows the phase diagrams M_s^{def} vs. J, where we can notice that the passing states are predominant. For $\rho = 40$ nm, there are two different states, skirting and pinning, both for small current densities and where the interaction force with the defect is maximum. The absence of other dynamical states can be attributed to the low influence of this magnetic parameter on the skyrmionium-defect interaction (Fig. 2 (g–h)). The interaction energy corresponding to M_s^{def} is an order of magnitude lower than the interaction energies of the other physical parameters of the defect.

Finally, in Fig. 4, we show how a sequence of magnetic defects can be used to modify the trajectory of the skyrmionium throughout its movement.

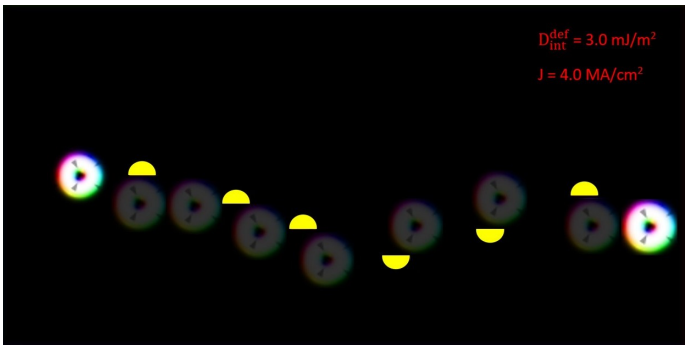

FIG. 4. Diagram of the trajectory followed by a skyrmionium along the racetrack in the presence of a sequence of magnetic defects (yellow semicircles)

4. Conclusions

We have shown how modifying the magnetic properties of a defect makes it possible to manipulate a skyrmionium along a racetrack. We calculated the interaction energies between the skyrmionium and the defect, considering different physical parameters of the defect and obtaining attractive and repulsive potentials depending on the physical parameters of the defect. Furthermore, we studied how these magnetic defects influence the dynamics of the skyrmionium. The magnetic defects that produce attractive potentials can be used as pinning centers to stop the movement of the skyrmionium. In contrast, magnetic defects with repulsive potentials can be used as skyrmionium dispersal centers. Our work may be of interest in using magnetic defects to modify the trajectory of a skyrmionium, which could find applications in creating logic gates in potential applications in the area of spintronics.

A. Appendix

A.1. Skyrmionium-magnetic defect interaction energy

Interaction energies were obtained using eq. (1) as given in the main article. Each term of the equation was obtained using the MuMax [31] built-in function relax, which calculates the system ground state. The origin of the coordinates is located in the center of the racetrack.

A.1.1. Skyrmionium–semicircular magnetic defect interaction energy with a width of $W = 512$ *nm.*

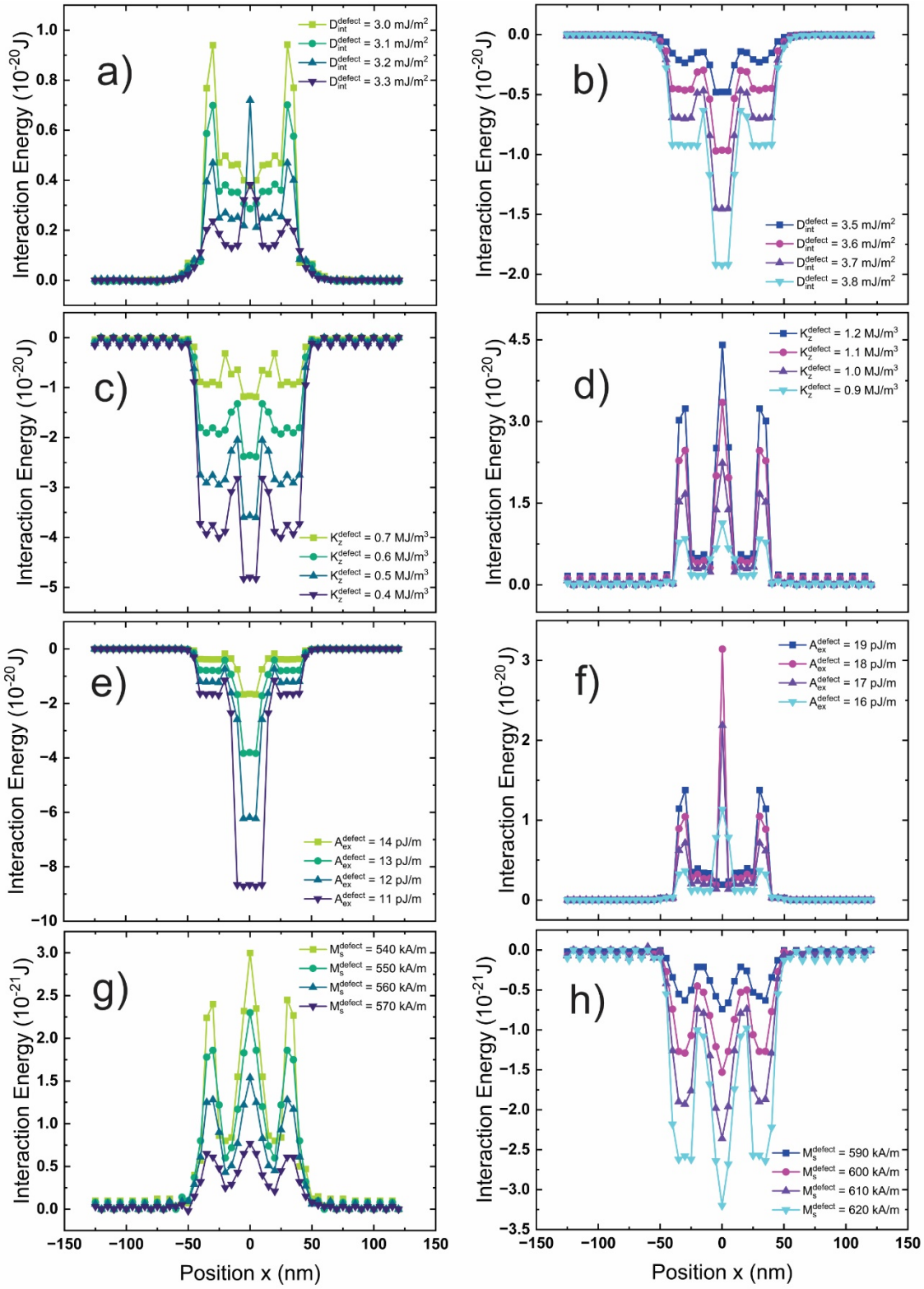

FIG. A1. Interaction energy between the skyrmionium and the defect ($\rho = 20$ nm) obtained by micromagnetic simulation using eq. (1) considering different defect parameters with a width of $W = 512$ nm

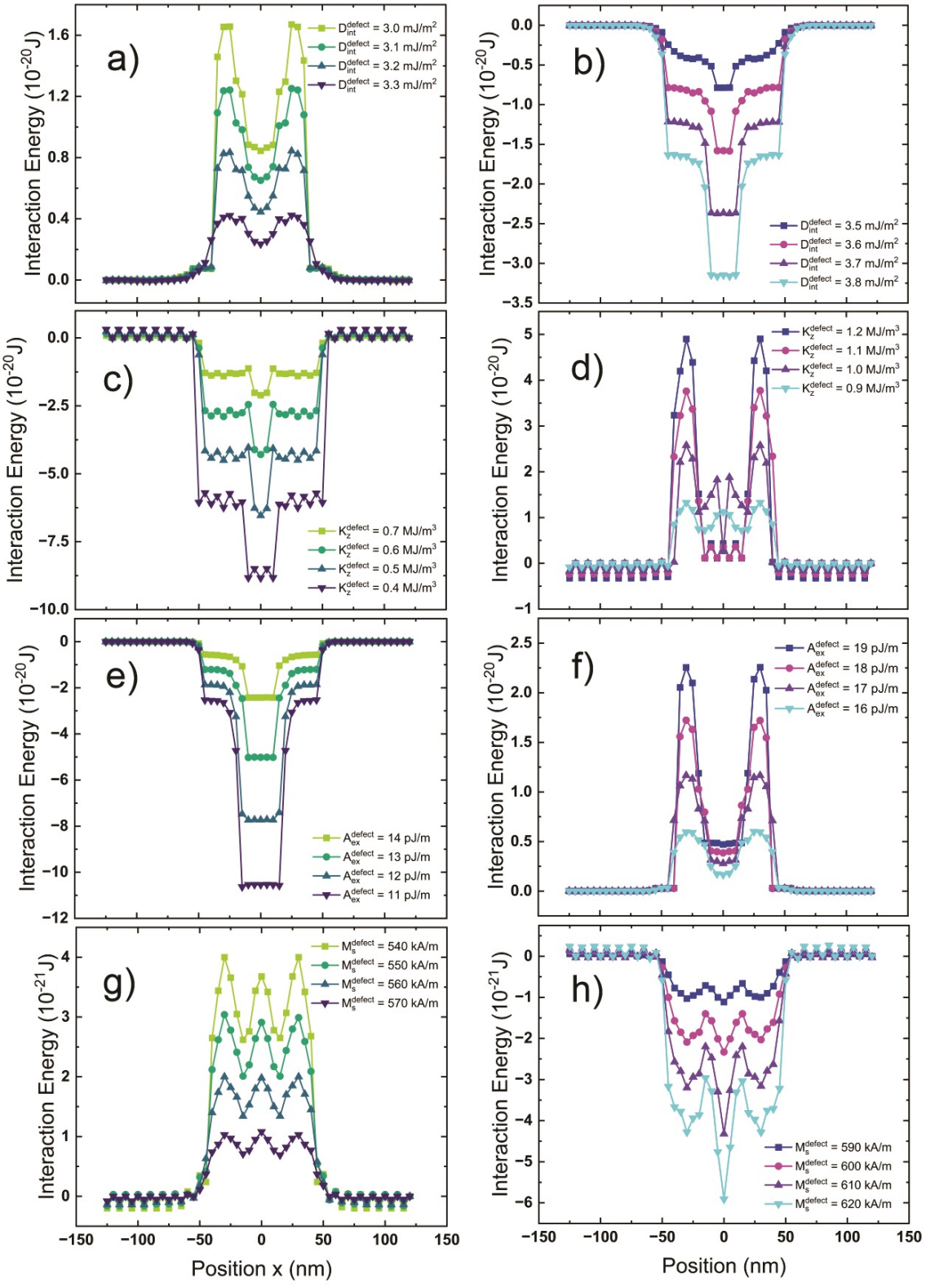

FIG. A2. Interaction energy between the skyrmionium and the defect ($\rho = 30$ nm) obtained by micromagnetic simulation using eq. (1) considering different defect parameters with a width of $W = 512$ nm

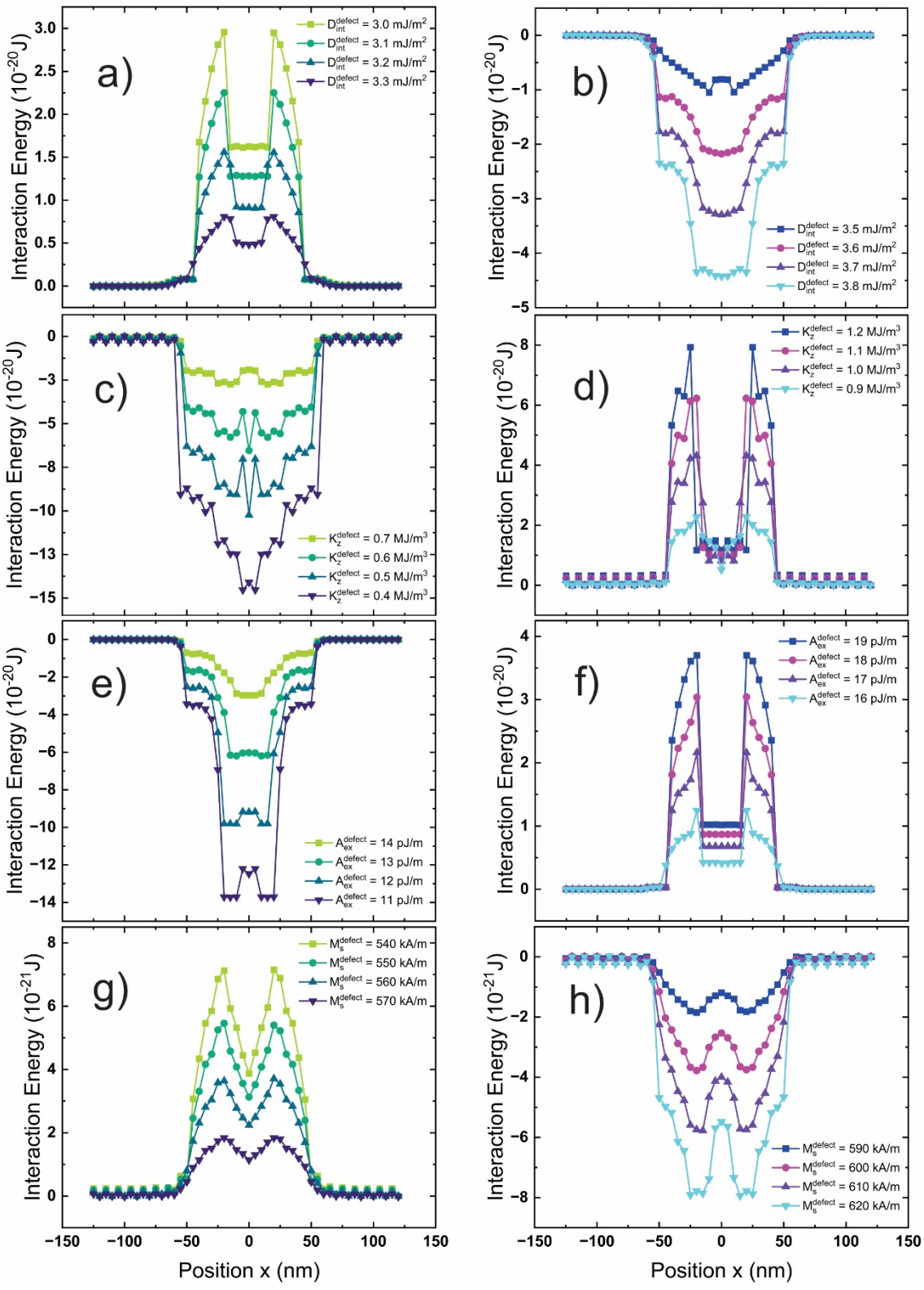

FIG. A3. Interaction energy between the skyrmionium and the defect ($\rho = 40$ nm) obtained by micromagnetic simulation using eq. (1), considering different defect parameters with a width of $W = 512$ nm

A.1.2. Skyrmionium-semicircular magnetic defect interaction energy with a width of $W = 256$ nm.

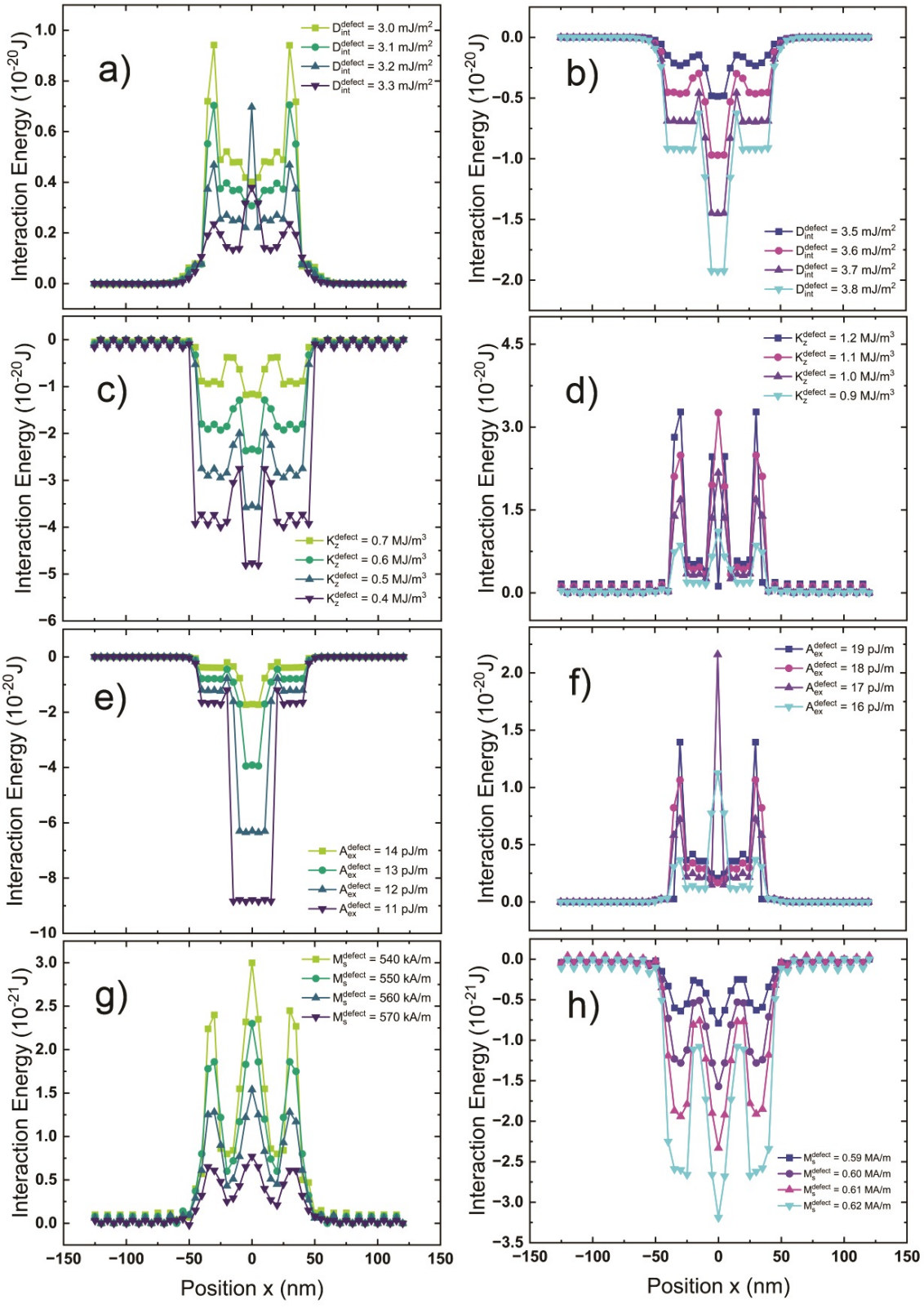

FIG. A4. Interaction energy between the skyrmionium and the defect ($\rho = 20$ nm) obtained by micromagnetic simulation using eq. (1) considering different defect parameters with a width of $W = 256$ nm

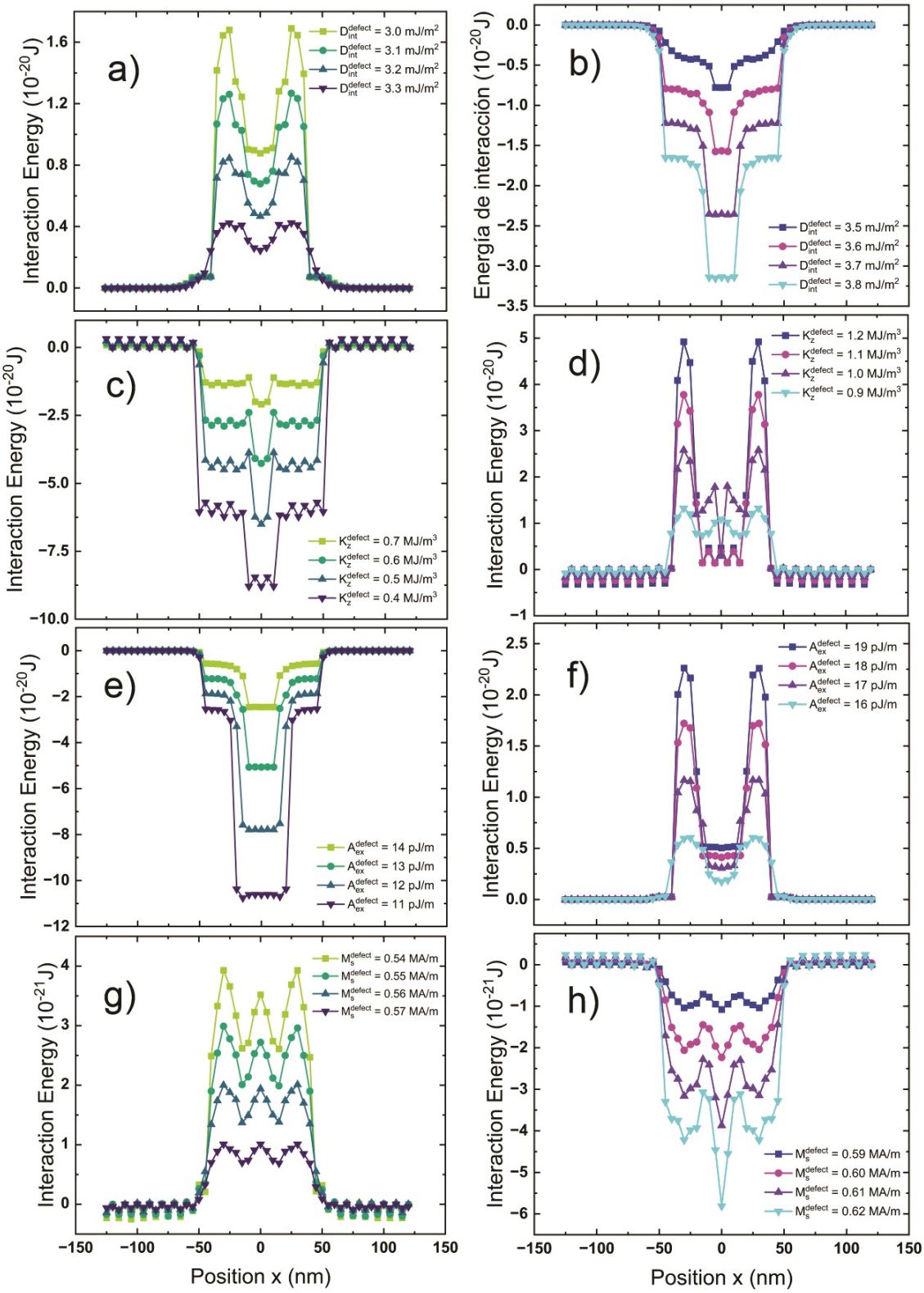

FIG. A5. Interaction energy between the skyrmionium and the defect ($\rho = 30$ nm) obtained by micromagnetic simulation using eq. (1) considering different defect parameters with a width of $W = 256$ nm

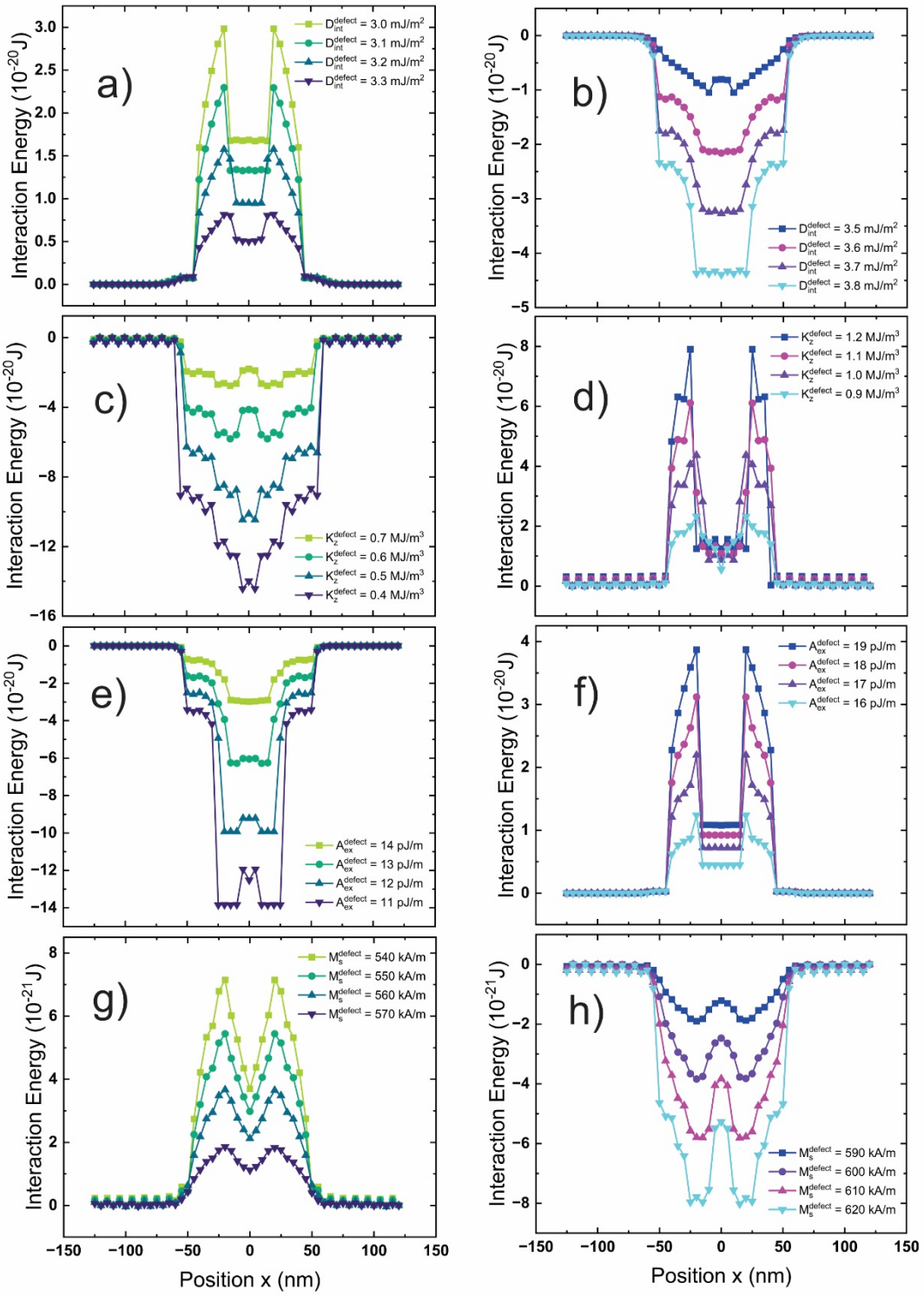

FIG. A6. Interaction energy between the skyrmionium and the defect ($\rho = 40$ nm) obtained by micromagnetic simulation using eq. (1) considering different defect parameters with a width of $W = 256$ nm

A.1.3. Skyrmionium–semicircular magnetic defect interaction energy with a width of $W = 128$ nm.

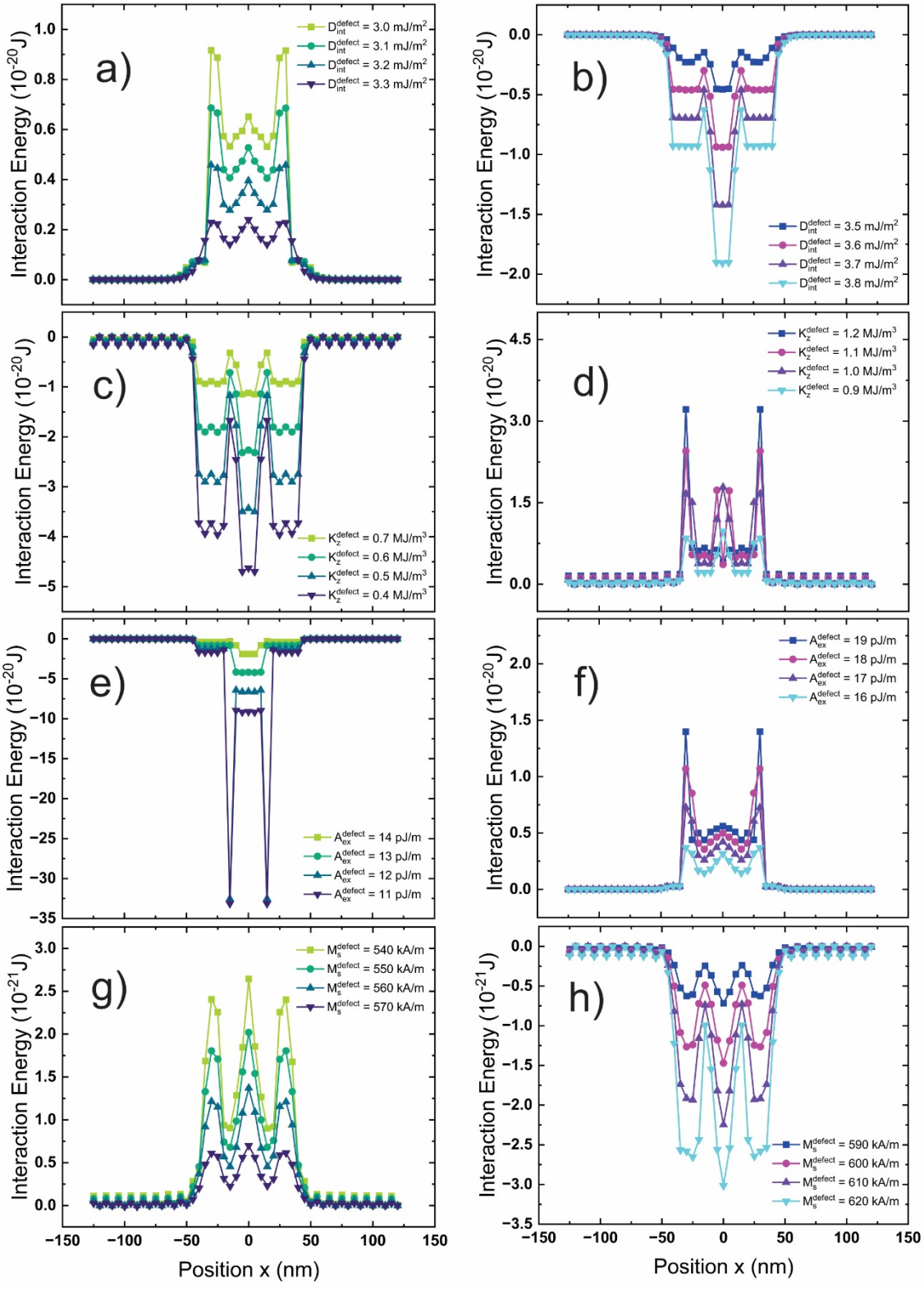

FIG. A7. Interaction energy between the skyrmionium and the defect ($\rho = 20$ nm) obtained by micromagnetic simulation using eq. (1) considering different defect parameters with a width of $W = 128$ nm

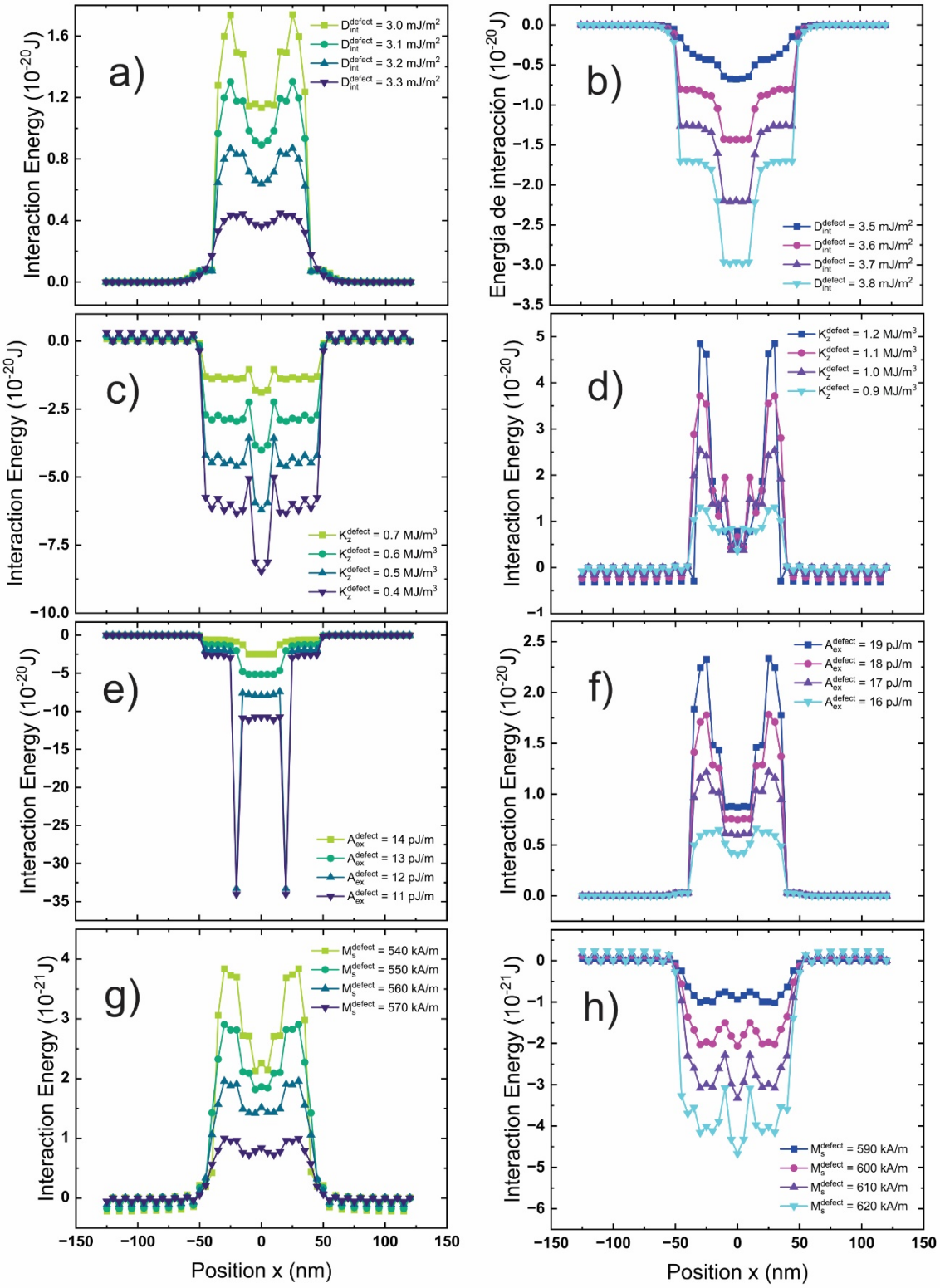

FIG. A8. Interaction energy between the skyrmionium and the defect ($\rho = 30$ nm) obtained by micromagnetic simulation using eq. (1) considering different defect parameters with a width of $W = 128$ nm

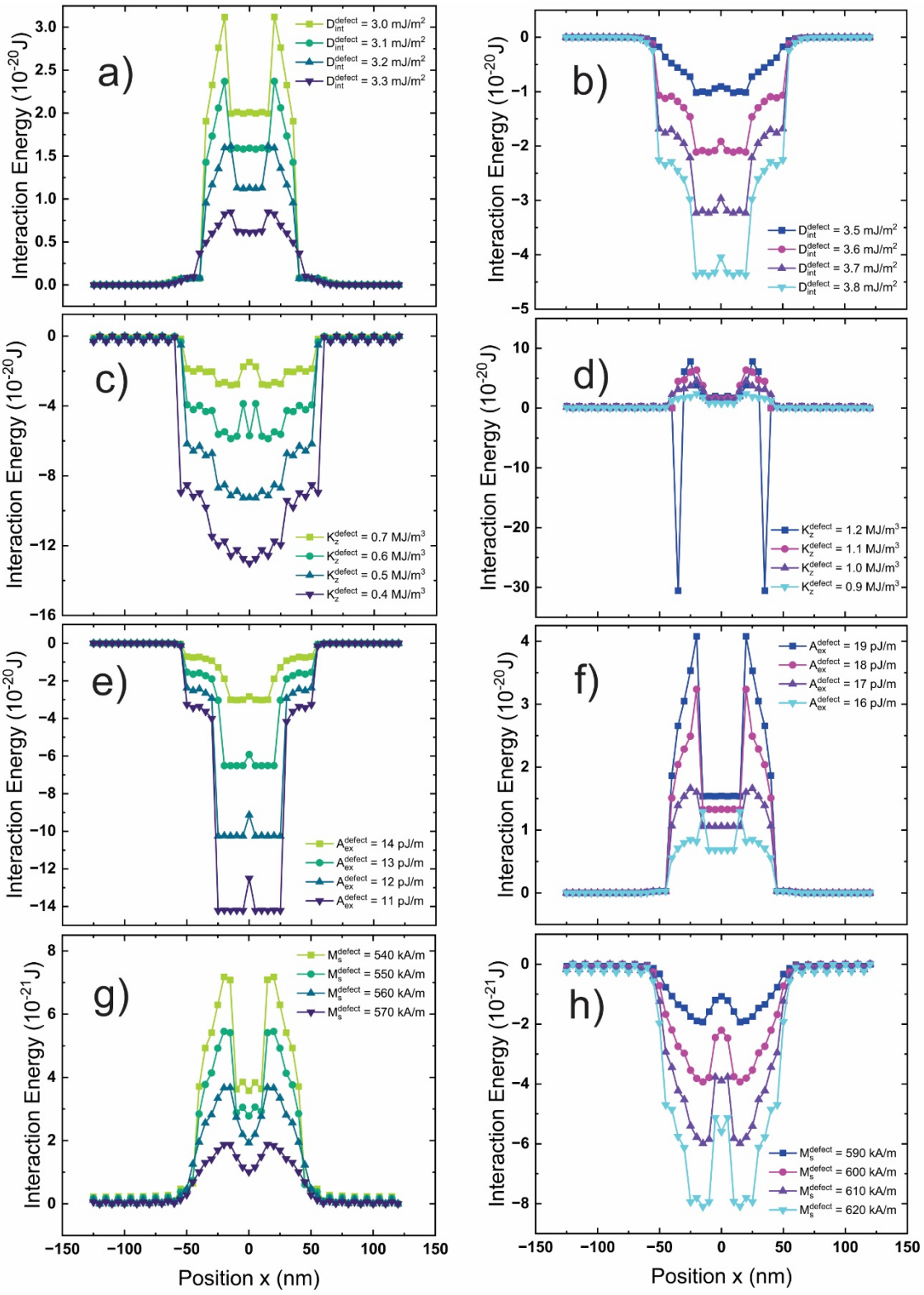

FIG. A9. Interaction energy between the skyrmionium and the defect ($\rho = 40$ nm) obtained by micromagnetic simulation using eq. (1) considering different defect parameters with a width of $W = 128$ nm

A.2. Phase diagrams for different values for the width W

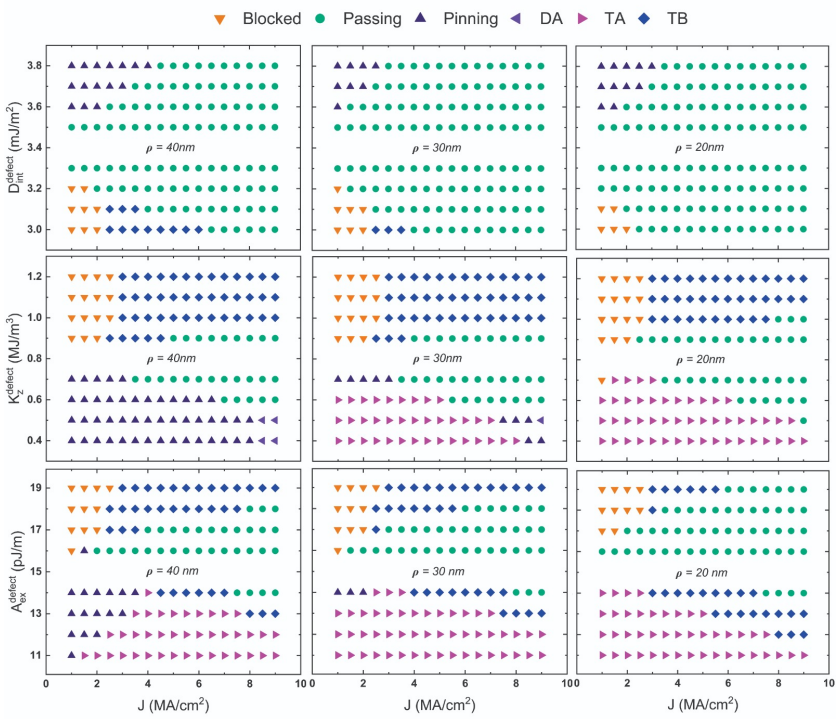

FIG. A10. The phase diagrams of possible states for the skyrmionium dynamics in the presence of a magnetic defect depict a wide range of physical parameters and diameters, offering a comprehensive view of the system's behavior for a width $W = 128$ nm

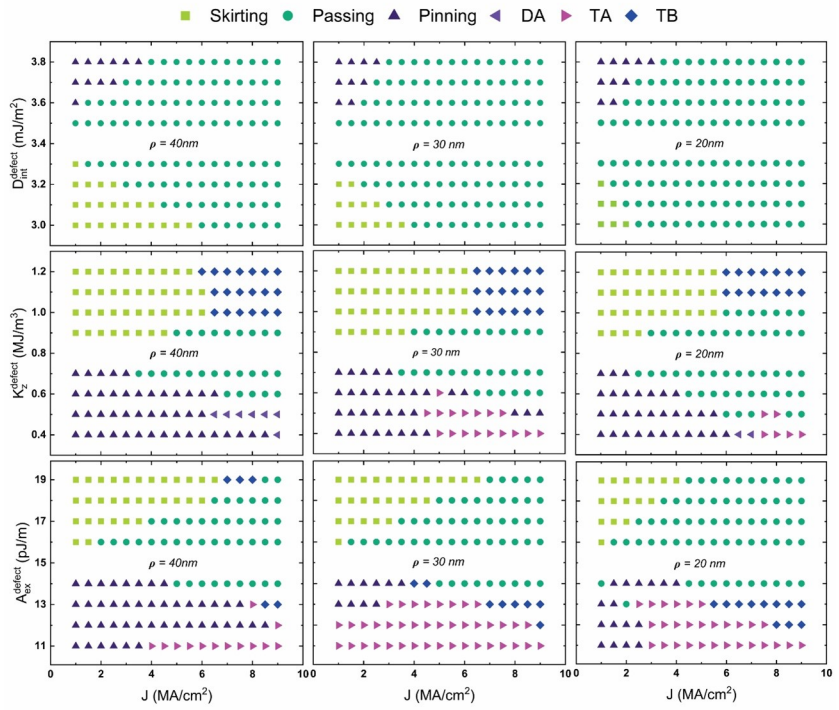

FIG. A11. The phase diagrams of possible states for the skyrmionium dynamics in the presence of a magnetic defect depict a wide range of physical parameters and diameters, offering a comprehensive view of the system's behavior for a width $W = 256$ nm

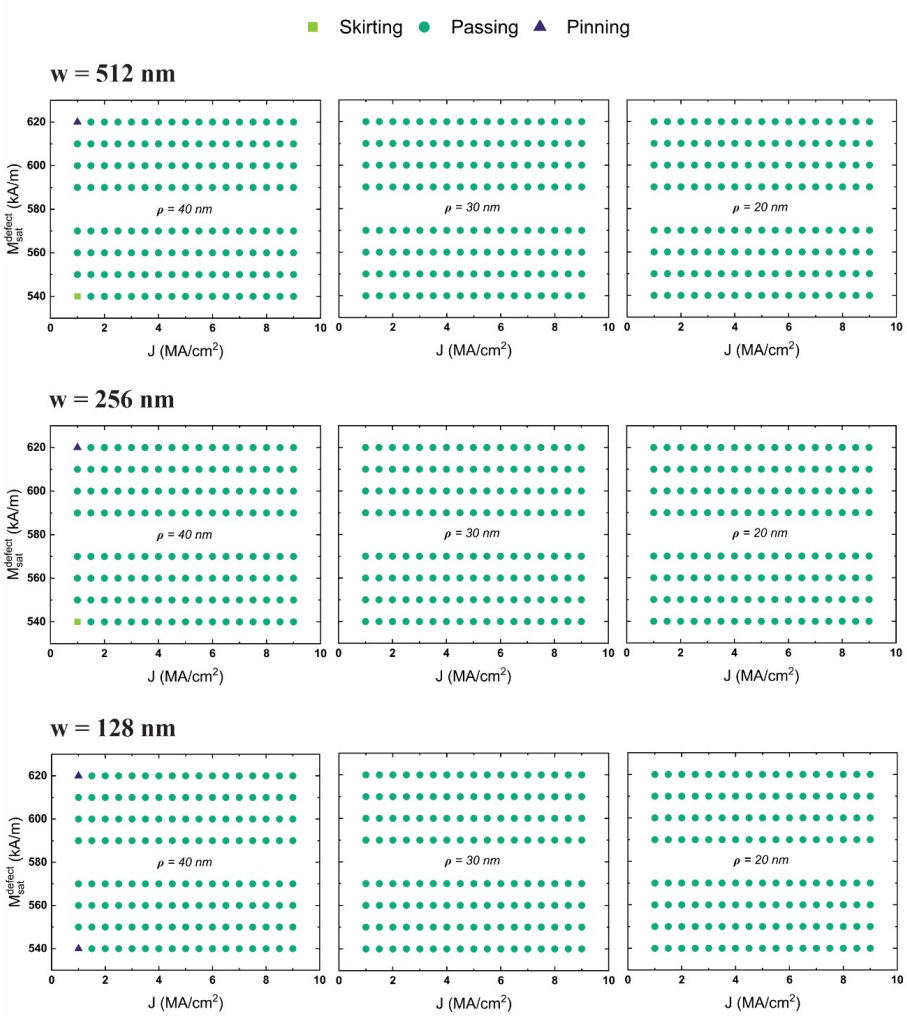

FIG. A12. Phase diagrams showing all possible skyrmionium dynamics states in the presence of a defect, with its saturation magnetization value $M_{\text{sat}}^{\text{defect}}$, for different widths ($W$) and diameters ($\rho$)

A.3. Schematic representation of different skyrmionium dynamics states

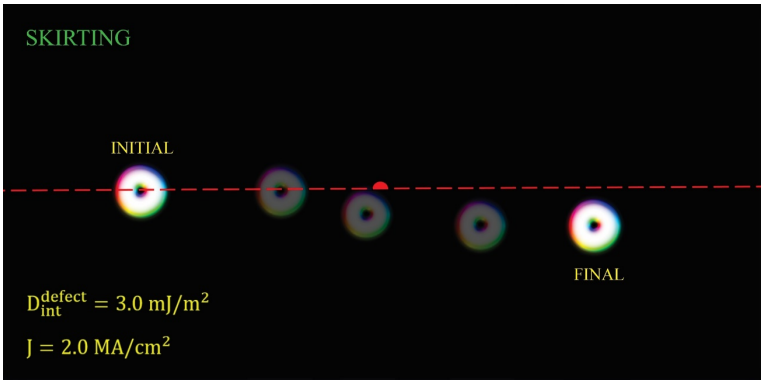

FIG. A13. Representation of the skirting state in which the skyrmionium avoids the magnetic defect to continue its movement along the racetrack

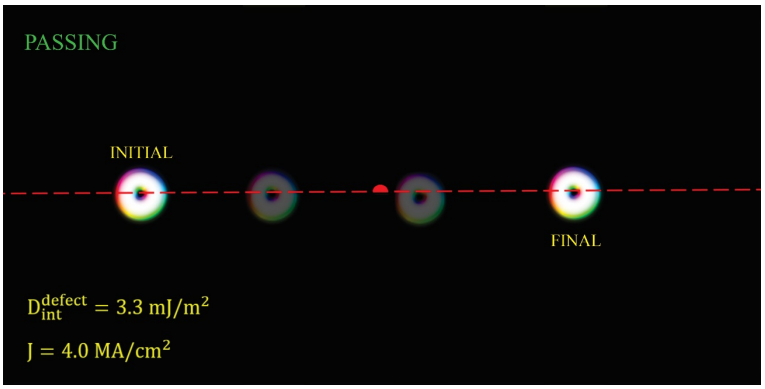

FIG. A14. Representation of the passing state in which the skyrmionium manages to cross the magnetic defect to continue its path along the racetrack

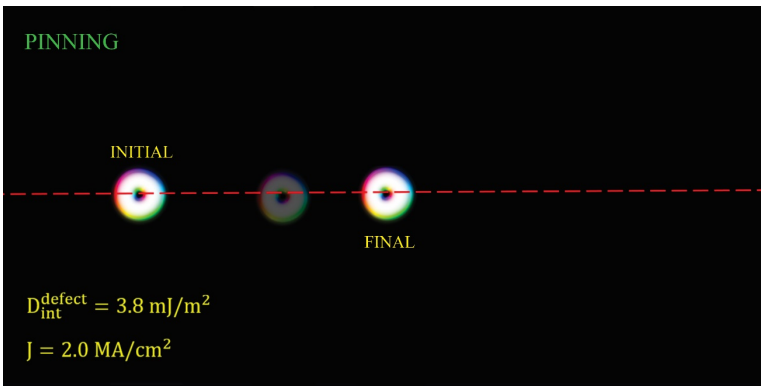

FIG. A15. Representation of the pinning state in which the skyrmionium is trapped inside the magnetic defect

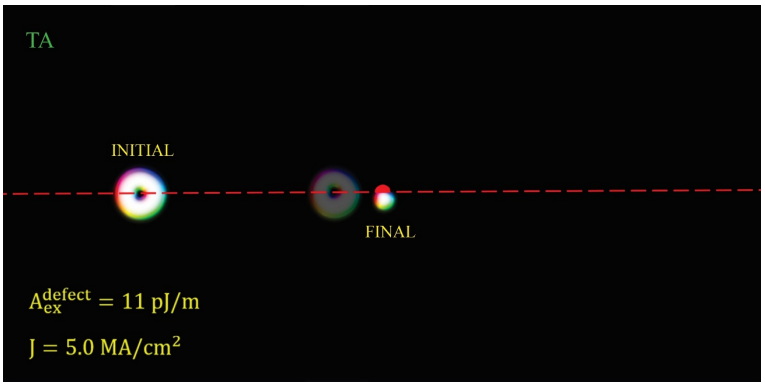

FIG. A16. Representation of the TA state in which a skyrmionium collapses into the defect, transforming into a skyrmion and becoming trapped within the defect

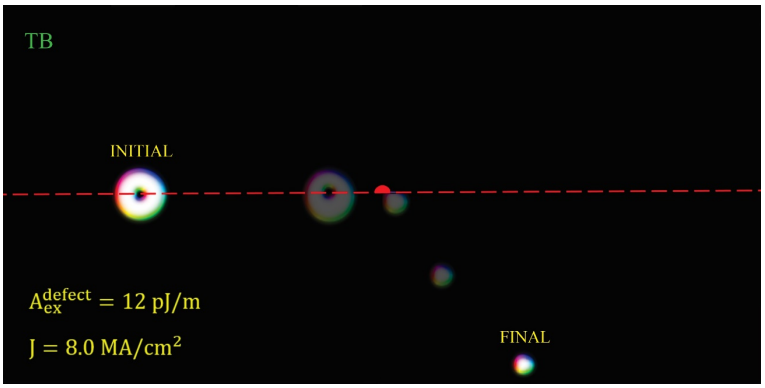

FIG. A17. Schematic representation of a skyrmionium collapsing into a defect, transforming to a skyrmion, and changing path from its original trajectory

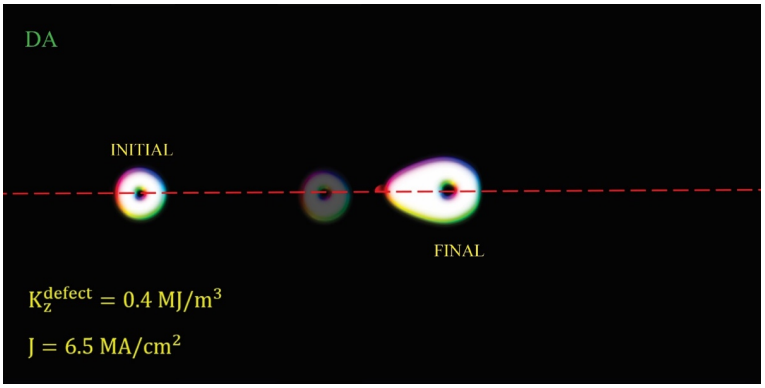

FIG. A18. A schematic representation shows a skyrmionium trapped by a defect. However, due to the current's effect, it deforms and increases in size along the racetrack

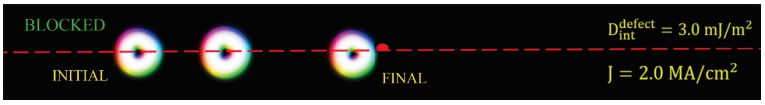

FIG. A19. Schematic representation of the blocked state; the skyrmionium stops before colliding with the defect

A.4. Skyrmion–magnetic defect interaction energy

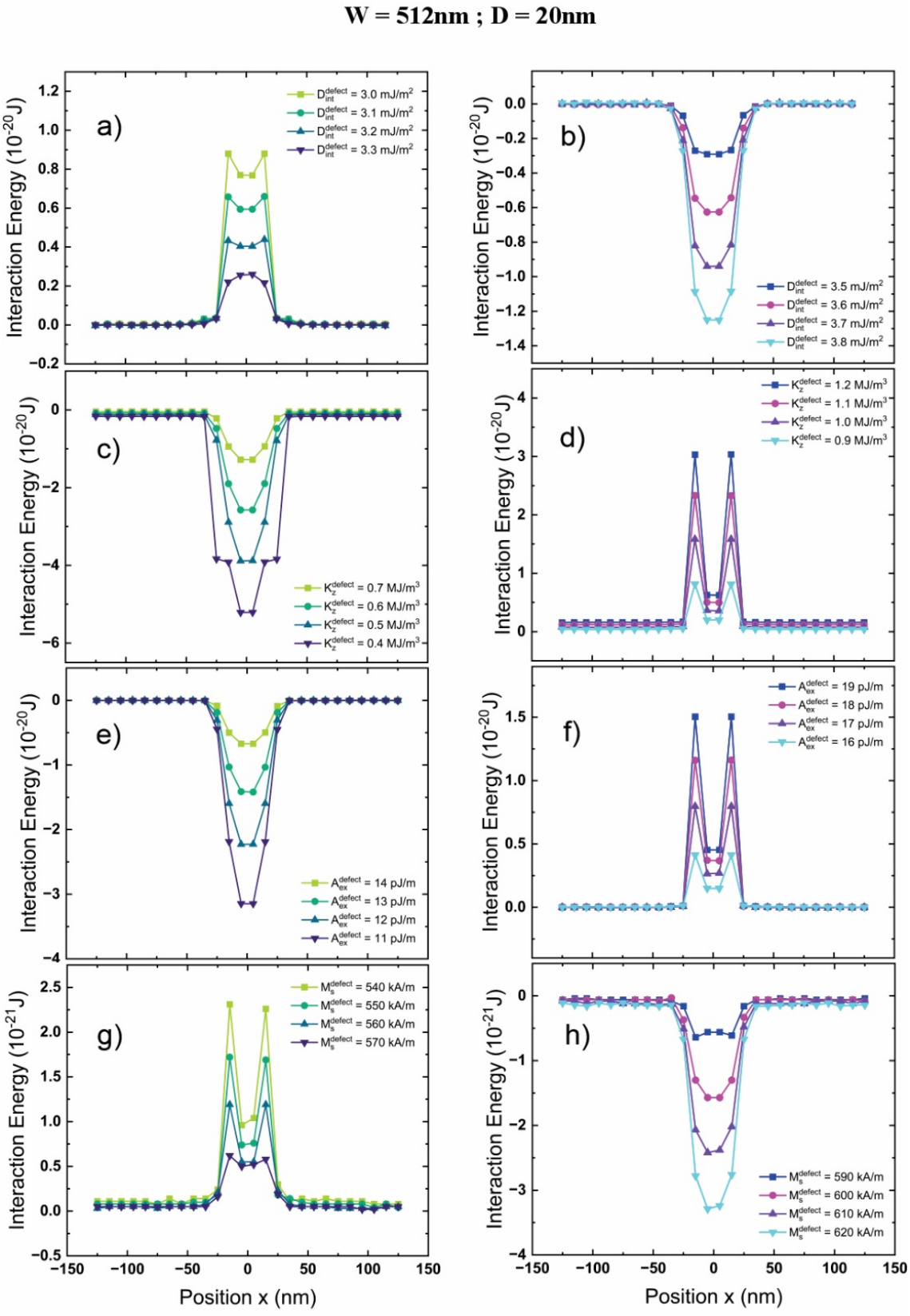

FIG. A20. Interaction energy between the skyrmion and the defect ($\rho = 20$ nm) obtained by micromagnetic simulation using eq. (1) considering different defect parameters with a width of $W = 512$ nm

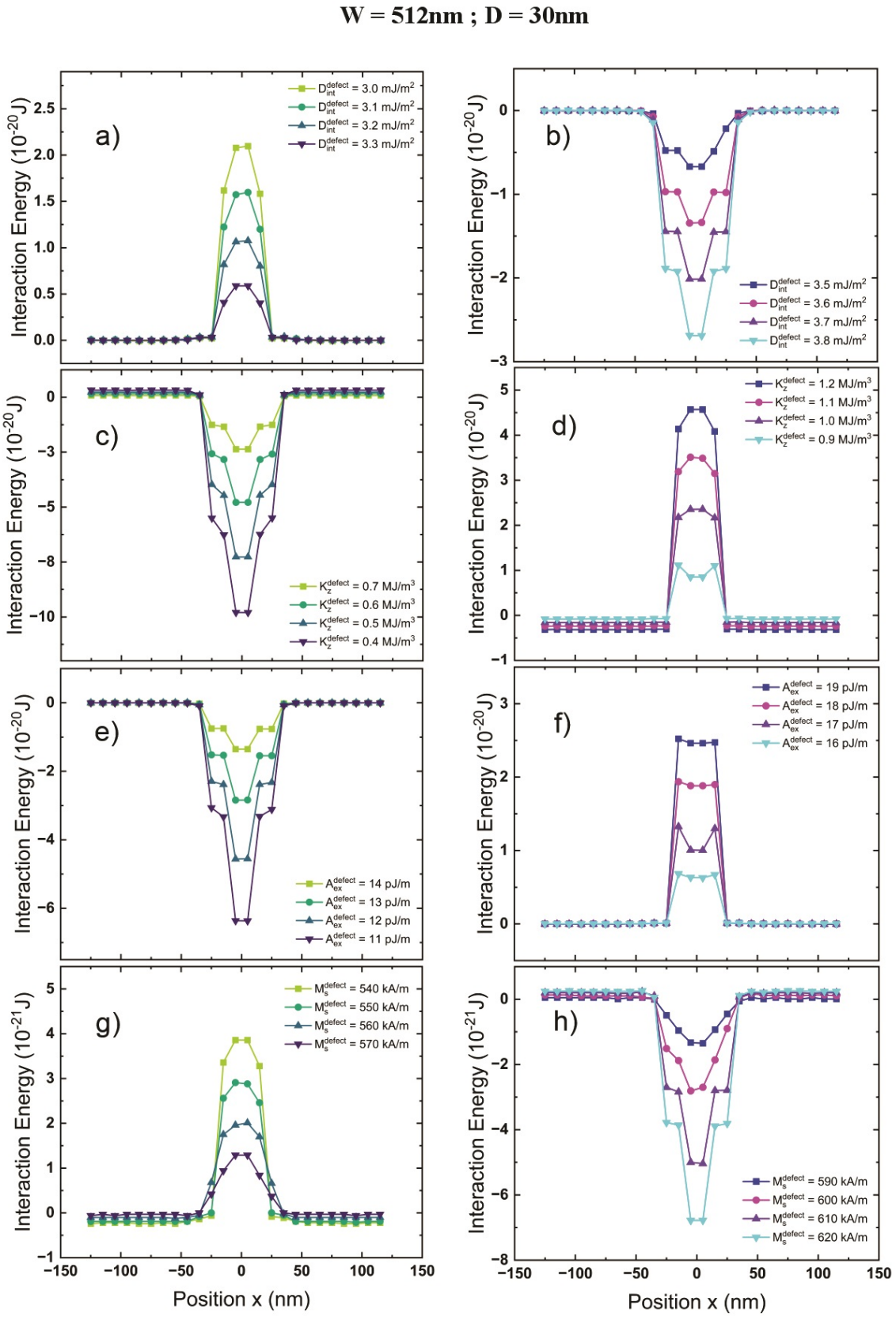

FIG. A21. Interaction energy between the skyrmion and the defect ($\rho = 30$ nm) obtained by micromagnetic simulation using eq. (1) considering different defect parameters with a width of $W = 512$ nm

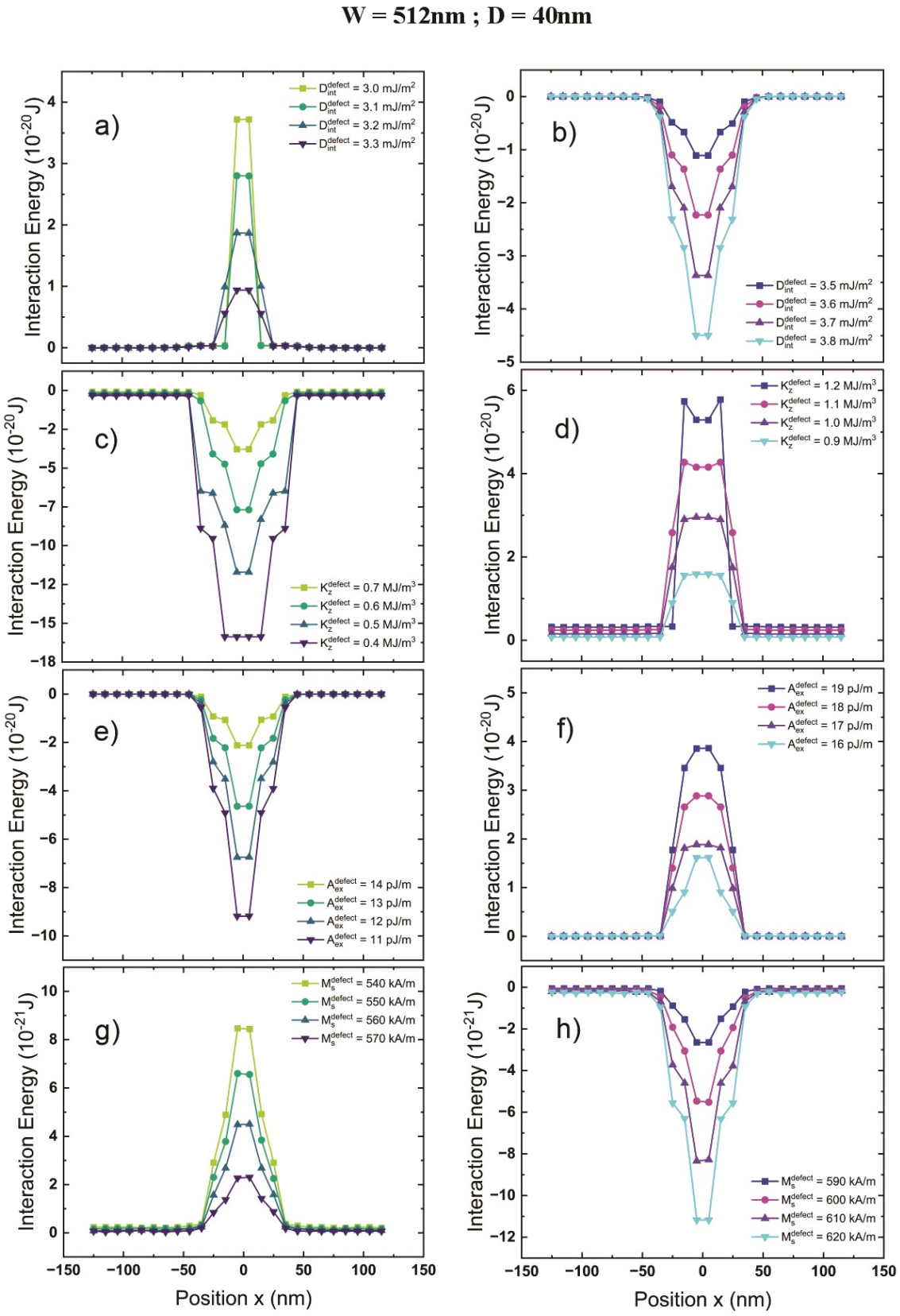

FIG. A22. Interaction energy between the skyrmion and the defect ($\rho = 40$ nm) obtained by micromagnetic simulation using eq. (1) considering different defect parameters with a width of $W = 512$ nm

References

[1] Göbel B., Mertig I., Tretiakov O.A. Beyond skyrmions: Review and perspectives of alternative magnetic quasiparticles. *Physics Reports*, 2021, **895**, P. 1–28.

[2] Jin C., Song C., Wang J., Liu Q. Dynamics of antiferromagnetic skyrmion driven by the spin Hall effect. *Applied Physics Letters*, 2016, **109** (18), 182404.

[3] Göbel B., Schäffer A.F., Berakdar J., Mertig I., Parkin S.S. Electrical writing, deleting, reading, and moving of magnetic skyrmioniums in a racetrack device. *Scientific reports*, 2019, **9** (1), 12119.

[4] Li S., Xia J., Zhang X., Ezawa M., Kang W., Liu X., Zhou Y., Zhao, W. Dynamics of a magnetic skyrmionium driven by spin waves. *Applied Physics Letters*, 2018, **112** (14), 142404.

[5] Novak R.L., Garcia F., Novais E.R.P., Sinnecker J.P., Guimaraes A.P. Micromagnetic study of skyrmion stability in confined magnetic structures with perpendicular anisotropy. *J. of Magnetism and Magnetic Materials*, 2018, **451**, P. 749–760.

[6] Beg M., Carey R., Wang W., Cortés-Ortuño D., Vousden M., Bisotti M. A., Albert M., Chernyshenko D., Hovorka O., Stamps R.L., Fangohr H. Ground state search, hysteretic behaviour, and reversal mechanism of skyrmionic textures in confined helimagnetic nanostructures. *Scientific Reports*, 2015, **5** (1), 17137.

[7] Ponsudana M., Amuda R., Madhumathi R., Brinda A., Kanimozhi N. Confinement of stable skyrmionium and skyrmion state in ultrathin nanoring. *Physica B*, 2021, **618**, 413144.

[8] Zhang X., Xia, J., Zhou Y., Wang, D., Liu X., Zhao, W., Ezawa M. Control and manipulation of a magnetic skyrmionium in nanostructures. *Physical Review B*, 2016, **94** (9), 094420.

[9] Tejo F., Riveros A., Escrig J., Guslienko K.Y., Chubykalo-Fesenko O. Distinct magnetic field dependence of Néel skyrmion sizes in ultrathin nanodots. *Scientific Reports*, 2018, **8** (1), 6280.

[10] Jiang W., Zhang X., Yu G., Zhang W., Wang X., Benjamin Jungfleisch M., Pearson J.E., Heinonen O., Wang K.L., Zhou Y., Hoffmann A., Te Velthuis S.G. Direct observation of the skyrmion Hall effect. *Nature Physics*, 2017, **13**, P. 162–169.

[11] Yanes R., Garcia-Sanchez F., Luis R.F., Martinez E., Raposo V., Torres L., Lopez-Diaz L. Skyrmion motion induced by voltage-controlled in-plane strain gradients. *Applied Physics*, 2019, **115** (13), 132401.

[12] Zhu H., Xiang G., Feng Y., Zhang X. Dynamics of elliptical magnetic skyrmion in defective racetrack. *Nanomaterials*, 2024, **14** (3), 312.

[13] Sampaio J., Cros V., Rohart S., Thiaville A., Fert A. Nucleation, stability and current-induced motion of isolated magnetic skyrmions in nanostructures. *Nature Nanotechnology*, 2013, **8** (11), P. 839–844.

[14] Fert A., Cros V., Sampaio J. Skyrmions on the track. *Nature Nanotech.*, 2013, **8** (3), P. 152–156.

[15] Lima Fernandes I., Bouaziz J., Blügel S., Lounis S. Universality of defect-skyrmion interaction profiles. *Nature Communication*, 2018, **9** (1), 4395.

[16] Toscano D., Leonel S.A., Coura P.Z., Sato F. Building traps for skyrmions by the incorporation of magnetic defects into nanomagnets: Pinning and scattering traps by magnetic properties engineering. *J. of Magnetism and Magnetic Materials*, 2019, **480**, P. 171–185.

[17] Lin J.Q., Chen J.P., Tan Z.Y., Chen Y., Chen Z.F., Li W.A., Gao X.S., Liu J.M. Manipulation of Skyrmion Motion Dynamics for Logical Device Application Mediated by Inhomogeneous Magnetic Anisotropy. *Nanomaterials*, 2022, **12** (2), 278.

[18] Toscano D., Mendonça J.P.A., Miranda A.L.S., de Araujo C.I.L., Sato F., Coura P.Z., Leonel S.A. Suppression of the skyrmion Hall effect in planar nanomagnets by the magnetic properties engineering: Skyrmion transport on nanotracks with magnetic strips. *J. of Magnetism and Magnetic Materials*, 2020, **504**, 166655.

[19] Kolesnikov A.G., Stebliy M.E., Samardak A.S., Ognev A.V. Skyrmionium–high velocity without the skyrmion Hall effect. *Scientific Reports*, 2018, **8** (1), 16966.

[20] Zheng F., Li H., Wang S., Song D., Jin C., Wei W., Kovács A., Zang J., Tian M., Zhang Y., Du H., Dunin-Borkowski R.E. Direct Imaging of a Zero-Field Target Skyrmion and Its Polarity Switch in a Chiral Magnetic Nanodisk. *Physical Review Letters*, 2017, **119** (9), 197205.

[21] Can Önel A., Çimen M., Yarimbiyik A.E., Arikan M., Rameev B. Interaction of a magnetic skyrmionium with an engineered defect. *J. of Superconductivity and Novel Magnetism*, 2023, **36** (6), P. 1533–1539.

[22] Chen R., Li Y., Pavlidis V.F., Moutafis C. Skyrmionic interconnect device. *Physical Review Research*, 2020, **2** (4), 043312.

[23] Song C., Ma Y., Jin C., Wang J., Xia H., Wang J., Liu Q. Field-tuned spin excitation spectrum of $k\pi$ skyrmion. *New J. of Physics*, 2019, **21** (8), 083006.

[24] Vigo-Cotrina H., Guimarães A.P. Creating skyrmions and skyrmioniums using oscillating perpendicular magnetic fields. *J. of Magnetism and Magnetic Materials*, 2020, **507**, 166848.

[25] Ishida Y., Kondo K. Theoretical comparison between skyrmion and skyrmionium motions for spintronics applications. *Japanese J. of Applied Physics*, 2020, **59**, SGGI04.

[26] Komineas S., Papanicolaou N. Skyrmion dynamics in chiral ferromagnets. *Physical Review B*, 2015, **92** (6), 064412.

[27] Song C., Jin C., Wang J., Ma Y., Xia H., Wang J., Xia H., Wang J., Liu Q. Dynamics of a magnetic skyrmionium in an anisotropy gradient. *Applied Physics Express*, 2019, **12** (8), 083003.

[28] Jiang A., Zhou Y., Zhang X., Mochizuki M. Transformation of a skyrmionium to a skyrmion through the thermal annihilation of the inner skyrmion. *Physical Review Research*, 2024, **6** (1), 013229.

[29] Kuchkin V.M., Kiselev N.S., Rybakov F.N., Lobanov I.S., Blügel S., Uzdin V.M. Heliknoton in a film of cubic chiral magnet. *Frontiers in Physics*, 2023, **11**, 1201018.

[30] Vigo-Cotrina H., Navarro-Vilca S., Urcia-Romero S. Skyrmionium dynamics on a racetrack in the presence of a magnetic defect. *J. of Applied Physics*, 2024, **135** (16), 163903.

[31] Vansteenkiste A., Leliaert J., Dvornik M., Helsen M., Garcia-Sanchez F., Van Waeyenberge B. The design and verification of MuMax3. *AIP Advances*, 2014, **4** (10), 107133.

Submitted 7 August 2024; revised 25 August 2024; accepted 26 August 2024

Information about the authors:

Sebastian Rodrigo Navarro Vilca – Departamento de Física Aplicada, Universidad Nacional Jorge Basadre Grohmann, Avenida Miraflores, S/N, Ciudad Universitaria, Tacna 23003, Perú; ORCID 0009-0000-8508-0406; srnavarrov@unjbg.edu.pe

Silvana Rocio Urcia Romero – Department of Physics, University of Puerto Rico, Mayagüez, Puerto Rico 00681, USA; ORCID 0000-0002-0730-9081; silvana.urcia@upr.edu

Helmunt Eduardo Vigo Cotrina – Grupo de Investigación en Ciencias Aplicadas y Nuevas Tecnologías, Universidad Privada del Norte, Trujillo, Perú; ORCID 0000-0003-4335-8777; helmunt.vigo@upn.edu.pe

Conflict of interest: the authors declare no conflict of interest.